Proceedings of the 21st ICSMGE, Vienna, Austria, 14 – 19 June 2026. Pistrol, Adam & Schweiger (eds.)
Published by: ÖGG, Austrian Society for Geomechanics, Salzburg, Austria, ISBN 978-3-9503898-4-5
https://doi.org/10.53243/ICSMGE2026-1362

Recent advances in material point method for geotechnical earthquake engineering

Zhi Lyu, Gang Wang
State Key Laboratory of Climate Resilience for Coastal Cities, Department of Civil & Environmental Engineering, The Hong Kong University of Science and Technology, Hong Kong S.A.R., China
gwang@ust.hk

ABSTRACT: The Material Point Method (MPM) has been gaining popularity in geotechnical engineering due to its advantages in simulating large deformations. However, several numerical challenges hinder its application in seismic analysis, which include difficulties to impose dynamic boundary conditions, substantial computational demands, sophisticated constitutive models to capture nonlinear dynamic soil behaviors, and challenges in handling soil-structure interactions. In response to these issues, this study introduces some recent advances at HKUST to improve MPM for geotechnical earthquake engineering applications. Firstly, a high-order hierarchical meshing scheme is developed to account for the multiscale mesh resolutions required for wave propagation and local shear band formation for analyzing dynamically induced large deformations in soils, thereby significantly reducing computational cost. Secondly, a framework for applying the traction-based dynamic boundary conditions, such as periodic boundary, transmitting boundary and free-field boundary, is also proposed. The scheme is further extended to accommodate oblique seismic wave incidence. Additionally, a multiphase MPM contact algorithm is introduced to simulate interactions between saturated soils and structures, enabling dynamic analysis of soil-structure interaction in liquefied grounds. Finally, we present various examples, including seismic slope failure, soil liquefaction-induced tunnel uplift and building collapse, to highlight these advancements and capabilities of MPM in solving challenging geotechnical earthquake engineering problems.

KEYWORDS: Material point method, numerical simulation, geotechnical earthquake engineering, soil-structure interaction.

1 INTRODUCTION

For the deformation analysis in geotechnical earthquake engineering, simplified methods such as empirical regressions (Swaisgood, 2003) and Newmark sliding block models (Rathje and Bray, 2000; Bray and Travasarou, 2007) cannot capture complex soil behaviors and post-failure mechanisms. While some mesh-based numerical methods (e.g., FEM and FDM) equipped with advanced constitutive models provide more comprehensive predictions, the issue of mesh distortion limits their applicability to large deformations.

The Material Point Method (MPM) (Sulsky et al., 1994), as a hybrid Eulerian-Lagrangian method, is well-suited for large deformation problems. Lagrangian particles discretize the material domain and carry state variables, while the Eulerian grid facilitates differentiation and integration. At the beginning of a typical calculation step, the information stored at material points (e.g., mass and velocity) is extrapolated to grids. Then, after solving the governing equations at nodes, the evolved nodal kinematic fields are interpolated back to particles for advection and updating stresses according to specific material models. Because of similarities to FEM and convenient incorporation of history-dependent soil models (Soga et al., 2016), MPM has been widely applied to various geotechnical large deformation analysis, such as landslides (Ceccato et al., 2024) and cone penetration tests (Fetrati et al., 2024).

However, the utilization of MPM in earthquake geotechnical engineering remains limited. It is cumbersome to impose proper dynamic boundary conditions in MPM, although some efforts have been made (Feng et al., 2021; Kohler et al., 2022; Alsardi and Yerro, 2023; Kurima et al., 2025). Another challenge is to deal with significant multi-resolution contradiction between shear band formation and wave propagation. For this issue, our group has proposed a multi-scale SEM-MPM framework and applied it to Hongshiyan landslide (Feng et al., 2022). Investigating soil liquefaction imposes additional demands on MPM, particularly requiring hydro-mechanical coupling algorithms and nonlinear dynamic soil models. Currently, only a handful of studies have addressed these challenges for liquefaction analysis using MPM (Giridharan et al., 2020; Feng et al., 2021; Alsardi and Yerro). Besides, seismic liquefaction frequently induces damage to structures, notably through building collapse and uplift of underground structures. Yet, seismic soil-structure-interaction analysis with MPM remains largely unaddressed due to the absence of the multiphase contact formulation.

This paper presents our recent advances addressing these gaps: 1) a higher-order mesh-grading strategy resolving multi-resolution issue in seismic failure, 2) a framework containing diverse traction-based dynamic boundary conditions (e.g., periodic, transmitting, and free-field boundaries) for simulating vertically or obliquely incident seismic waves, and 3) a multiphase contact formulation for soil-structure interaction (SSI) analysis. Subsequently, we use some representative cases for validation and showing capability of the proposed methods. Final concluding remarks are summarized in the end.

2 EHANCEMENTS OF MPM FOR SEISMIC ANALYSIS

2.1 *Higher order mesh-grading MPM*

Seismic failures often involve highly localized deformations, so it is common in FEM and FDM to refine the spatial resolution within the potential failure zone. Traditional MPM usually adopts uniform Cartesian grids for the sake of simplicity, incurring excessive computational costs. Existing mesh-grading approaches (Lian et al., 2015; Cheon and Kim, 2019)# mostly use linear shape functions prone to cell-crossing errors. Higher order shape functions such as B-splines (Steffen et al., 2008) and moving least squares (Hu et al., 2018) can mitigate errors, but it is tedious to develop mesh refinement based on them due to their non-local support property.

To overcome these constraints, we developed a higher-order mesh-grading MPM framework based on Generalized Interpolation Material Point (GIMP) formulation (Bardenhagen and Kober, 2004). Figure 1(a) gives an example of the hierarchical mesh, in which the particle spacing conforms to cell size. To achieve shape functions continuity at the interface of different level grids without cell-crossing error, the method employs GIMP C^1-continuous shape function as defined in Eq. (1):

$$S_{Ip} = \frac{1}{\Omega_p}\int_{\Omega_p} N_I(\boldsymbol{x})\chi_p(\boldsymbol{x})d\Omega, \tag{1}$$

where Ω_p is the volume of a particle, $N_I(\boldsymbol{x})$ is the local-support linear nodal weight function, and $\chi_p(\boldsymbol{x})$ is particle characteristic function in Heaviside form. For the non-conforming interface as illustrated in Figure 1(b), the coarser cell connected with refined mesh zone serves as transition layer and virtually split into finer cells. Then, the virtual nodes are introduced for data transfer between computational nodes and particles, and they are tied to transition cells. For the example in Figure 1(b), the interface nodes, including *F*, *G*, *H* and *I*, are attached to the middle coarse cell, and they have no real degrees of freedom (DOFs). Based on such tie constraints, the shape functions of interface nodes can be implicitly reformulated as the combination of these virtual nodes (Gao et al., 2017), which avoids complicated explicit forms for the element with variable nodes (Lian et al., 2015). It is noted that we retain DOFs of hanging nodes (e.g., Node E in Figure 1(b)) in this work despite removability. This paper adopts explicit time integration with universal time step determined by the smallest cell size, while the multi-time step scheme (Sun et al., 2020) is worth exploring in the future.

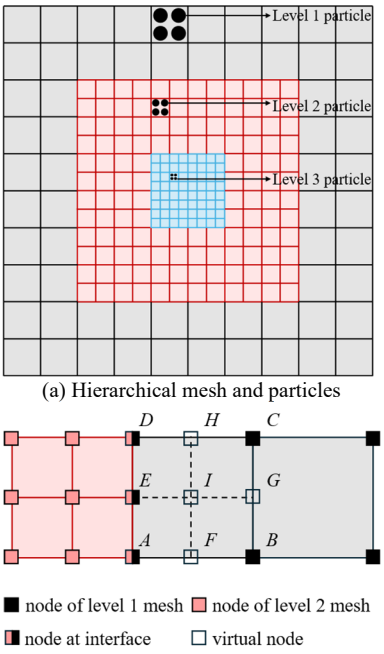

(a) Hierarchical mesh and particles

(b) Transition layer for continuity

Figure 1. Mesh-grading MPM scheme.

2.2 *Dynamic boundary conditions and earthquake input*

Artificial dynamic boundaries are vital for seismic modeling, which are utilized to input ground motions and suppress spurious wave reflections at truncated domain boundaries. Our traction-based framework for seismic large deformation analysis integrates several popular dynamic boundary conditions, including periodic boundaries, free-field boundaries and transmitting boundaries.

The periodic boundaries (Zienkiewicz et al., 1999) in FEM are also called *tied degrees of freedom* (e.g., in PLAXIS) and *EqualDOF* (e.g., in OpenSees), indicating that the lateral sides of the model are enforced to have identical displacements. In MPM, a penalty method is employed. We connect lateral boundary particles via stiff springs, while converting such penalty forces to equivalent tractions.

For models without periodic surface perturbation, the free-field boundaries should be applied. A typical slope model under vertically propagating plane wave is shown in Figure 2(a). As seen, periodic boundaries are imposed on the free-field columns to attain 1D dynamic responses in the far field. These responses should be coupled to the main domain through Lysmer dashpots (Lysmer and Kuhlemeyer, 1969). Hence, the tractions on the lateral boundaries can be written as Eqs. (2) and (3):

$$\bar{f}_x^{side} = -\rho c_p\left(v_x^m - v_x^{ff}\right) + \bar{f}_x^{ff,dyn} + \bar{f}_x^{st}, \tag{2}$$

$$\bar{f}_y^{side} = -\rho c_s\left(v_y^m - v_y^{ff}\right) + \bar{f}_y^{ff,dyn} + \bar{f}_y^{st}, \tag{3}$$

where ρ is material density; c_p and c_s are the shear and dilative wave speeds of material, respectively; $v_{\square}^{ff}$ are velocities of free-field; $\bar{f}_{\square}^{ff,dyn}$ are the tractions contributed from dynamic stresses in free field; $\bar{f}_{\square}^{st}$ are the tractions due to the static stresses of the model.

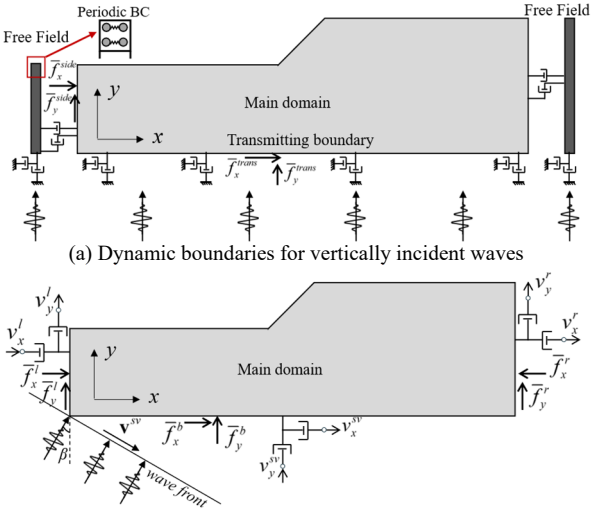

(a) Dynamic boundaries for vertically incident waves

(b) Generalized dynamic boundaries for obliquely incident waves

Figure 2. Traction-based dynamic boundaries and earthquake input.

At the model base, transmitting boundaries utilize analogous tractions for earthquake input. Specifically, the tractions on the base with normal direction in *y* as depicted in Figure 2(a) can be given as Eqs. (4) and (5):

$$\bar{f}_y^{trans} = -\rho c_p\left(v_y^m - 2v_{dil}^{inp}\right) + \bar{f}_y^{st}, \tag{4}$$

$$\bar{f}_x^{trans} = -\rho c_s\left(v_x^m - 2v_{shear}^{inp}\right) + \bar{f}_x^{st}, \tag{5}$$

where v_{dil}^{inp} and v_{shear}^{inp} are velocities of input dilative wave and shear wave, respectively.

So far, the dynamic problems under vertically incident seismic waves, as shown in Figure 2(a), can be simulated. However, it is well-known that non-vertically incident seismic waves are more realistic, especially for shallow earthquake or near-field problems (Huang and Wang, 2015). Some studies stated that larger incident angle can cause more intense topographic amplifications (Ashford and Sitar, 1997; Chen et al., 2019). Thus, we generalized the traction-based boundary conditions to accommodate oblique incidence. Figure 2(b) shows a slope under an obliquely incident SV-wave at angle β. The tractions at all boundaries, including lateral sides and bottom base, have a unified formulation (Chang et al., 2024; Shen et al., 2024), as described in Eq. (6):

$$\bar{f}_i^b = \bar{f}_i^{b,vis} + \bar{f}_i^{b,dyn} + \bar{f}_i^{b,st}, \tag{6}$$

where subscript *i* can be *x* and *y*, superscript *b* denotes boundary. It can be seen that the total tractions combine three components: $\bar{f}_i^{b,st}$ is used to maintain static equilibrium, $\bar{f}_i^{b,vis}$ represents viscous tractions to coordinate kinematics of free-field and lateral boundary, and $\bar{f}_i^{b,dyn}$ denotes the dynamic responses of

free-field. Clearly, Eqs. (2) to (5) can be covered by Eq. (6). The dynamic velocities and stresses at the bottom of the model are determined by the velocities of incident SV wave. For the lateral sides of the model, we compute the dynamic responses using analytical method based on wave potential theory (Zhao et al., 2019).

2.3 *Multiphase contact for SSI*

This study modified the widely employed grid-based contact method in MPM (Bardenhagen et al., 2000) to handle multi-phase interaction. We utilize the single-point two-phase MPM using $\mathbf{v}_s - \mathbf{v}_f$ formulation (Kafaji, 2013) for effective stress analysis of saturated soil, while the solid structure is modeled via classical single-phase MPM. Figure 3 illustrates the contact configuration between saturated soil and a structure, where s, f, and r denote soil skeleton, pore fluid, and structure, respectively. The green dots represent the nodes possessing multi-material fields, such as node I. Determining the interface normal direction, $\mathbf{n}^{\mathrm{r}}$ in Figure 3, plays an important role in contact computations, and this topic has been discussed in detail in the literature (Nairn, 2013; Nairn et al., 2020). Here, $\mathbf{n}^{\mathrm{r}}$ is defined as the outward normal from the structure to soil, computed by the volume gradient method. Contact mechanics should be triggered when objects are touching and compressing each other along this normal at multi- material nodes (Nairn, 2013).

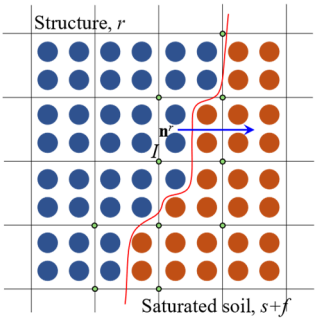

Figure 3. Illustration of contact between structure and saturated soil.

The multiphase contact scheme here can accommodate cohesionless Mohr-Coulomb type interface between soil and structure. It requires the enforcement of two constraints. The first one is continuity of normal velocities as suggested in single phase contact (Bardenhagen et al., 2000). This requires soil and structure share a common *center-of-mass velocity*, indicating $\mathbf{v}_I^s \cdot \mathbf{n}_I^r = \mathbf{v}_I^r \cdot \mathbf{n}_I^r$. In addition, the interface should be undrained, which means that the flux satisfies $q_I^n = (\mathbf{v}_I^f - \mathbf{v}_I^s) \cdot \mathbf{n}_I^r = 0$. Hence, combining these yields the post-contact normal velocities of all phases as Eq. (7):

$$\mathbf{v}_I^s \cdot \mathbf{n}_I^r = \mathbf{v}_I^f \cdot \mathbf{n}_I^r = \mathbf{v}_I^r \cdot \mathbf{n}_I^r = \frac{\mathbf{p}_I^s + \mathbf{p}_I^f + \mathbf{p}_I^r}{m_I^s + m_I^f + m_I^r} \cdot \mathbf{n}_I^r, \qquad (7)$$

where $m_I^{\square}$, $\mathbf{v}_I^{\square}$ and $\mathbf{p}_I^{\square}$ denote mass, velocity and momentum per phase at node I, respectively. Tangential behavior of the interface follows an effective stress based frictional contact model between soil skeleton and structure (Martinelli and Galavi, 2022).

3 NUMERICAL CASES

3.1 *Slope failures under obliquely incident SV wave*

The numerical model is illustrated in Figure 4(a), where the incident angle of SV wave is represented as β. This is a 10-meter-high sandy slope with 45° inclination. The three-level background mesh is set for MPM simulation, in which the finest grid size is 0.25m and the particle spacing varies from 0.125m to 0.5m. The acceleration time history of the incident SV wave is from Northridge earthquake records at Baldwin Hills, as shown in Figure 5. The elastoplastic slope follows a strain-softening Mohr-Coulomb model (Feng et al., 2021), with the material parameters listed in Table 1. To obtain the initial static equilibrium under gravity, the model bottom is fully fixed while the lateral sides of the model are only allowed to move vertically. Then, we remove all the constraints and switch to traction-based boundaries described in Section 2.2 for dynamic analysis.

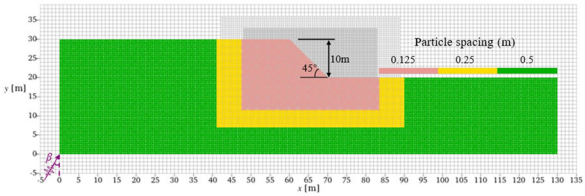

Figure 4. Mesh-grading MPM model of the slope failure subjected to obliquely incident wave with angle β.

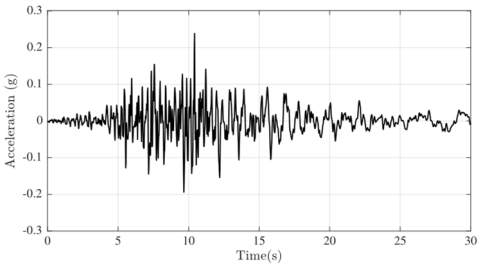

Figure 5. Acceleration time history of input wave from Northridge earthquake records at Baldwin Hills.

Table 1. Material properties for the slope under oblique SV waves

Parameter	Symbol	Value	Unit
Density	ρ	1700	kg/m^3
Young's modulus	E	40	MN/m^2
Poisson's ratio	v	0.28	-
Peak friction angle	φ^p	45	deg
Residual friction angle	φ^r	28	deg
Peak cohesion	c^p	4	kPa
Residual cohesion	c^r	0	kPa
Softening coefficient	η^s	15	-

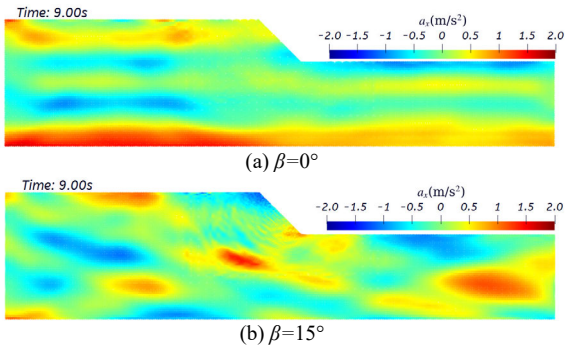

(a) β=0°

(b) β=15°

Figure 6. Horizontal accelerations of the slope under SV wave with different incident angles at t=9s.

Two incident angles are considered, which are β=0° and β=15°. The contours of horizontal acceleration for two cases at t=9s and t=13s are presented in Figure 6 and Figure 7, respectively. Wavefront patterns distinctly reflect incident angles: vertically incident waves (β=0°) generate nearly horizontal wavefronts parallel to the plain base, whereas

oblique incidence (β=15°) produces tilted wavefronts. This phenomenon is particularly clear when the slope has no evident failure, as shown in Figure 6. It is also found that responses are continuous across mesh levels, indicating the validity of mesh-grading approach.

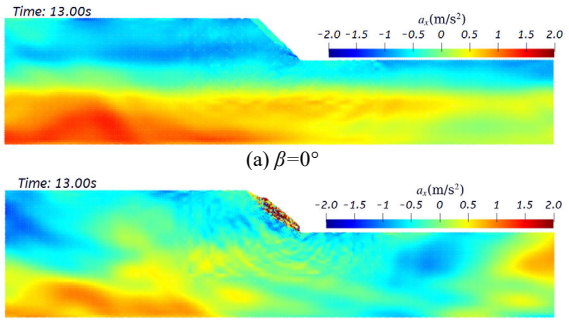

(a) β=0°

(b) β=15°

Figure 7. Horizontal accelerations of the slope under SV wave with different incident angles at t=13s.

Furthermore, the development of slope failure exhibits evident dependency on incident angle, and the oblique wave leads to earlier slope failure compared with the vertically propagated wave. As shown in Figure 7, for the incident angle of 0°, at 13 seconds the shear band is still developing, while the pronounced sliding has happened in the model of β=15°.

3.2 *Liquefaction-induced tunnel uplift*

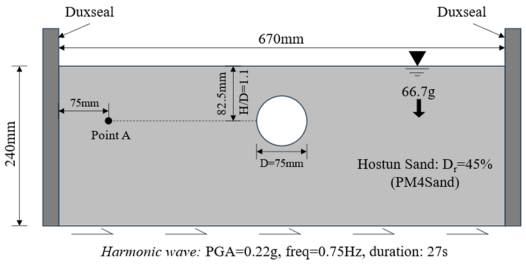

Harmonic wave: PGA=0.22g, freq=0.75Hz, duration: 27s

(a) Layout of centrifuge test in lab-scale (Chian et al., 2014)

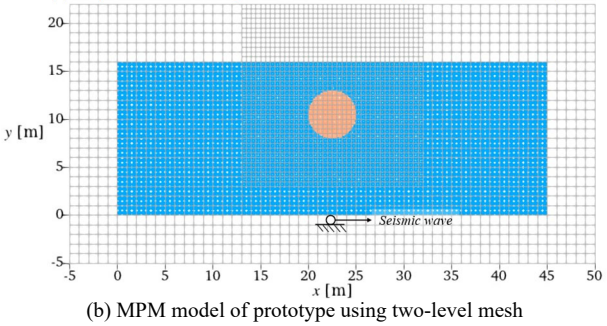

(b) MPM model of prototype using two-level mesh

Figure 8. Model of liquefaction induced tunnel uplift.

To demonstrate the capability of MPM for dynamic soil-structure interaction and liquefaction, a centrifuge test of the floatation of the underground structure (Chian et al., 2014) is simulated. The layout of the centrifuge model and the corresponding MPM model are illustrated in Figure 8. A circular tunnel is embedded in the saturated Hostun Sand of relative density 45%, and the model is subject to a harmonic wave whose peak ground acceleration (PGA) and frequency are 0.22g and 0.75Hz, respectively. The prototype-scale MPM model employs two-level mesh with refined grid size of 0.5m near the tunnel. The PM4Sand (Boulanger and Ziotopoulou, 2017) is used to model the dynamic nonlinear behavior of soil. The detailed material parameters are referred to related FEM and FDM studies (Rashiddel et al., 2024; Khateeb et al., 2025). The tunnel is modeled as a stiff elastic object whose density is around 300kg/m^3, and the friction coefficient of 0.4 is set for the soil-tunnel interface.

Figure 9 shows that the pore water pressure increases significantly during shaking compared to initial hydrostatic status, which is the cause of the soil liquefaction and provides buoyancy to uplift underground structures. As the tunnel goes up, the surrounding soil concurrently has upward movement. In contrast, some settlements are observed on the ground surface far from tunnel. Pore pressure continuity across mesh levels confirms the applicability of mesh-grading MPM to multiphase modeling.

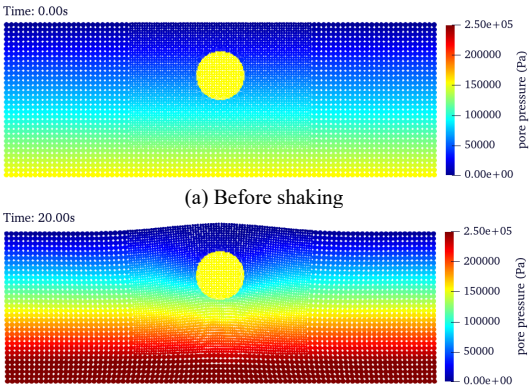

(a) Before shaking

(b) In shaking at t=20s

Figure 9. Contours of pore pressure distribution.

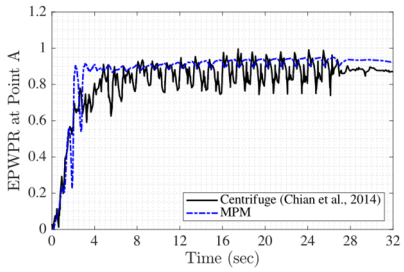

(a) Excess pore water pressure ratio time history at Point A

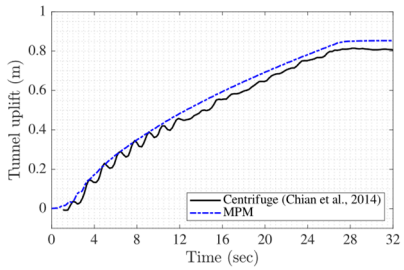

(b) Uplift displacement time history

Figure 10. Comparison of results between centrifuge test and MPM.

Figure 10 compares the time histories of the excess pore water pressure ratio (EPWPR) and tunnel uplift displacement between MPM and centrifuge results. At observation Point A labeled in Figure 8, EPWPR evolution proves the capability of PM4Sand in capturing the process of soil liquefaction, as seen in Figure 10(a). For the uplift displacement, MPM model accurately predicts both development and final magnitude, as depicted in Figure 10(b), validating the proposed multiphase contact method.

3.3 *Liquefaction-induced building collapse*

As illustrated in Figure 11, two adjacent structures with shallow foundations rest on the li quefiable ground: an 18-meter-high building and a 9-meter-high building separated by the gap of 2.5 meters. In this study, buildings and foundations are simplified as elastic blocks. Based on the literature (Kassas et

al., 2022), the equivalent density of buildings here is around 340kg/m^3. The ground is medium dense sand, modeled by PDMY03 (Khosravifar et al., 2018). A pseudo harmonic wave used in some centrifuge tests (Adamidis and Madabhushi, 2018) is employed as input excitation. The unform mesh with grid size of 0.5m is utilized for MPM simulation.

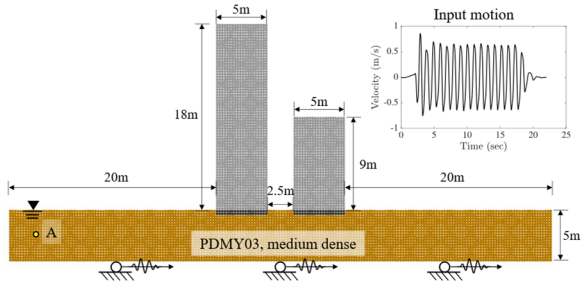

Figure 11. The model of adjacent buildings with shallow foundations on the liquefiable soil.

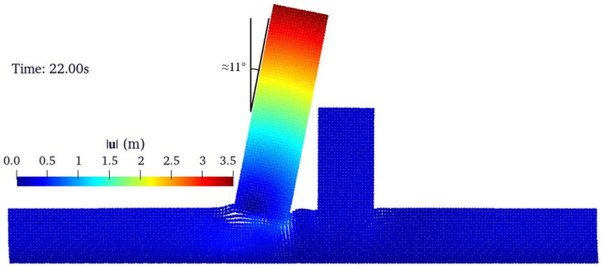

Figure 12. Contour of displacement magnitude at the end of shaking.

Post-shaking displacement contour, as shown in Figure 12, reveals distinct failure behaviors of two buildings. The left higher building has significantly collapsed to the right, with the tilt angle of around 11°. In contrast, the lower building on the right has almost no rotation, and only some settlements can be observed. Soil between the buildings bulges upward due to compression from such differential movements. Furthermore, the stress path of Point A (marked in Figure 11) confirms ground liquefaction during shaking, as depicted in Figure 13. Generally, the stress path is bounded within critical state lines showing butterfly shape, which indicates the soil dynamic properties are well captured by PDMY03.

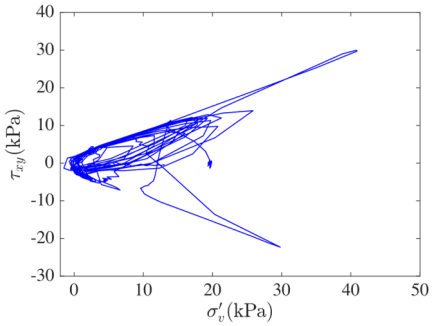

Figure 13. Stress path of Point A.

4 CONCLUSIONS

This paper has introduced some recent advances at HKUST to promote MPM to be a capable and versatile numerical tool for geotechnical earthquake engineering. A mesh-grading MPM based on GIMP is proposed to balance the computational cost and accuracy. A unified traction-based framework is developed to analyze the large deformation problems caused by the vertically or non-vertically incident seismic waves. In addition, the conventional contact method in MPM is modified for multiphase contact.

Then, some applications are provided to demonstrate our contributions, including the seismic slope failure under SV waves of different incident angles, soil liquefaction induced tunnel uplift and building collapse. It can be concluded that:

- Our numerical framework can simulate the whole process of seismic-induced landslides, including wave propagation and post-failure.
- The obliquely incident wave makes the slope slide earlier than the vertically incident wave.
- Mesh-grading MPM can be seamlessly incorporated into hydro-mechanical coupling analysis.
- The proposed multiphase contact method performs well in modeling of dynamic SSI during seismic liquefaction.
- MPM is capable of complicated seismic large deformation analysis, such as liquefaction induced building collapse.

5 ACKNOWLEDGEMENTS

The authors are grateful for the financial support from General Research Funds 16215823, 16219424, Theme-based Research Scheme T22-606/23-R from Hong Kong Research Grants Council (RGC), and ITC-SKLCRCC26EGP1 from State Key Laboratory of Climate Resilience for Coastal Cities at HKUST.

6 REFERENCES

Adamidis, O. and Madabhushi, S.P., 2018. Deformation mechanisms under shallow foundations on liquefiable layers of varying thickness. *Géotechnique*, 68(7), pp.602–613.

Alsardi, A. and Yerro, A., 2023. Coseismic site response and slope instability using periodic boundary conditions in the material point method. *Journal of Rock Mechanics and Geotechnical Engineering*, 15(3), pp.641–658.

Alsardi, A. and Yerro, A., 2024. MPM Coseismic Slope Runout Prediction Using the Intergranular Strain Anisotropy Hypoplastic Model. In: *Geo-Congress 2024*. American Society of Civil Engineers. pp.203–212.

Ashford, S.A. and Sitar, N., 1997. Analysis of topographic amplification of inclined shear waves in a steep coastal bluff. *Bulletin of the Seismological Society of America*, 87(3), pp.692–700.

Bardenhagen, S., Brackbill, J. and Sulsky, D., 2000. The material-point method for granular materials. *Computer methods in applied mechanics and engineering*, 187(3–4), pp.529–541.

Bardenhagen, S.G. and Kober, E.M., 2004. The generalized interpolation material point method. *Computer Modeling in Engineering and Sciences*, 5(6), pp.477–496.

Boulanger, R. and Ziotopoulou, K., 2017. *PM4Sand (Version 3.1): A sand plasticity model for earthquake engineering applications*. University of California, Davis, CA: Center for Geotechnical Modeling, Department of Civil and Environmental Engineering.

Bray, J.D. and Travasarou, T., 2007. Simplified procedure for estimating earthquake-induced deviatoric slope displacements. *Journal of geotechnical and geoenvironmental engineering*, 133(4), pp.381–392.

Ceccato, F., Yerro, A. and Carluccio, G.D., 2024. Simulating landslides with the material point method: Best practices, potentialities, and challenges. *Engineering Geology*, 338, p.107614.

Chang, C.-Y., Yang, W.-C. and Kuo, C.-H., 2024. Traction-based implementation of transmitting boundaries for nonlinear seismic Soil–Structure interaction analyses. *Soil Dynamics and Earthquake Engineering*, 179, p.108538.

Chen, Z., Huang, D., Wang, G. and Jin, F., 2019. Topographic amplification on hilly terrain under oblique incident waves. In: *Sustainable and Safe Dams Around the World/Un monde de barrages durables et sécuritaires*. CRC Press. pp.2778–2786.

Cheon, Y.-J. and Kim, H.-G., 2019. An adaptive material point method coupled with a phase-field fracture model for brittle materials. *International Journal for Numerical Methods in Engineering*, 120(8), pp.987–1010.

Chian, S.C., Tokimatsu, K. and Madabhushi, S.P.G., 2014. Soil liquefaction–induced uplift of underground structures: physical

and numerical modeling. *Journal of Geotechnical and Geoenvironmental Engineering*, 140(10), p.04014057.

Feng, K., Huang, D., Wang, G., Jin, F. and Chen, Z., 2022. Physics-based large-deformation analysis of coseismic landslides: A multiscale 3D SEM-MPM framework with application to the Hongshiyan landslide. *Engineering Geology*, 297, p.106487.

Feng, K., Wang, G., Huang, D. and Jin, F., 2021. Material point method for large-deformation modeling of coseismic landslide and liquefaction-induced dam failure. *Soil Dynamics and Earthquake Engineering*, 150, p.106907.

Fetrati, M., Galavi, V., Goodarzi, M., Mörz, T. and Kreiter, S., 2024. Simulation of cone penetrometer tests in sand using three advanced constitutive models: A comparative study. *Computers and Geotechnics*, 176, p.106683.

Gao, M., Tampubolon, A.P., Jiang, C. and Sifakis, E., 2017. An adaptive generalized interpolation material point method for simulating elastoplastic materials. *ACM Transactions on Graphics*, 36(6), pp.1–12.

Giridharan, S., Gowda, S., Stolle, D.F. and Moormann, C., 2020. Comparison of UBCSAND and hypoplastic soil model predictions using the material point method. *Soils and Foundations*, 60(4), pp.989–1000.

Hu, Y., Fang, Y., Ge, Z., Qu, Z., Zhu, Y., Pradhana, A. and Jiang, C., 2018. A moving least squares material point method with displacement discontinuity and two-way rigid body coupling. *ACM Transactions on Graphics (TOG)*, 37(4), pp.1–14.

Huang, D. and Wang, G., 2015. Region-specific spatial cross-correlation model for stochastic simulation of regionalized ground-motion time histories. *Bulletin of the Seismological Society of America*, 105(1), pp.272–284.

Kafaji, I., 2013. *Formulation of a Dynamic Material Point Method (MPM) for Geomechanical Problems*. PhD thesis. University of Stuttgart.

Kassas, K., Adamidis, O. and Anastasopoulos, I., 2022. Structure–soil–structure interaction (SSSI) of adjacent buildings with shallow foundations on liquefiable soil. *Earthquake Engineering & Structural Dynamics*, 51(10), pp.2315–2334.

Khateeb, S.D.A.A.-, Issa, M.J.K. and Seyedi, M., 2025. A Numerical Assessment of the Efficiency of Partial Saturation as a Countermeasure Against Liquefaction-Induced Uplift of Tunnels. *Journal of Earthquake Engineering*, 29(2), pp.547–570.

Khosravifar, A., Elgamal, A., Lu, J. and Li, J., 2018. A 3D model for earthquake-induced liquefaction triggering and post-liquefaction response. *Soil Dynamics and Earthquake Engineering*, 110, pp.43–52.

Kohler, M., Stoecklin, A. and Puzrin, A.M., 2022. A MPM framework for large-deformation seismic response analysis. *Canadian Geotechnical Journal*, 59(6), pp.1046–1060.

Kurima, J., Chandra, B. and Soga, K., 2025. Absorbing boundary conditions in material point method adopting perfectly matched layer theory. *Soil Dynamics and Earthquake Engineering*, 191, p.109219.

Lian, Y.P., Yang, P.F., Zhang, X., Zhang, F., Liu, Y. and Huang, P., 2015. A mesh-grading material point method and its parallelization for problems with localized extreme deformation. *Computer Methods in Applied Mechanics and Engineering*, 289, pp.291–315.

Lysmer, J. and Kuhlemeyer, R.L., 1969. Finite dynamic model for infinite media. *Journal of the engineering mechanics division*, 95(4), pp.859–877.

Martinelli, M. and Galavi, V., 2022. An explicit coupled MPM formulation to simulate penetration problems in soils using quadrilateral elements. *Computers and Geotechnics*, 145, p.104697.

Nairn, J., 2013. Modeling imperfect interfaces in the material point method using multimaterial methods. *Comput. Model. Eng. Sci*, 1(1), pp.1–15.

Nairn, J.A., Hammerquist, C.C. and Smith, G.D., 2020. New material point method contact algorithms for improved accuracy, large-deformation problems, and proper null-space filtering. *Computer Methods in Applied Mechanics and Engineering*, 362, p.112859.

Rashiddel, A., Abedi, M., Dias, D. and Ramesh, A., 2024. Seismic analysis of segmental shallow tunnels adjacent to building foundations under soil liquefaction and its mitigation. *Soil Dynamics and Earthquake Engineering*, 178, p.108479.

Rathje, E.M. and Bray, J.D., 2000. Nonlinear coupled seismic sliding analysis of earth structures. *Journal of Geotechnical and Geoenvironmental Engineering*, 126(11), pp.1002–1014.

Shen, H., Liu, Y., Li, H., Liu, B., Xia, X. and Yu, C., 2024. Numerical evaluation of ground motion amplification of rock slopes under obliquely incident seismic waves. *Soil Dynamics and Earthquake Engineering*, 178, p.108488.

Soga, K., Alonso, E., Yerro, A., Kumar, K. and Bandara, S., 2016. Trends in large-deformation analysis of landslide mass movements with particular emphasis on the material point method. *Géotechnique*, 66(3), pp.248–273.

Steffen, M., Kirby, R.M. and Berzins, M., 2008. Analysis and reduction of quadrature errors in the material point method (MPM). *International journal for numerical methods in engineering*, 76(6), pp.922–948.

Sulsky, D., Chen, Z. and Schreyer, H.L., 1994. A particle method for history-dependent materials. *Computer methods in applied mechanics and engineering*, 118(1–2), pp.179–196.

Sun, Z., Gan, Y., Huang, Z. and Zhou, X., 2020. A local grid refinement scheme for B-spline material point method. *International Journal for Numerical Methods in Engineering*, 121(11), pp.2398–2417.

Swaisgood, J., 2003. Embankment dam deformations caused by earthquakes. In: *Pacific conference on earthquake engineering*.

Zhao, W., Chen, W., Yang, D., Tan, X., Gao, H. and Li, C., 2019. Earthquake input mechanism for time-domain analysis of tunnels in layered ground subjected to obliquely incident P-and SV-waves. *Engineering Structures*, 181, pp.374–386.

Zienkiewicz, O.C., Chan, A., Pastor, M., Schrefler, B. and Shiomi, T., 1999. *Computational geomechanics with special reference to earthquake engineering*. John Wiley & Sons.